Advances in Science and Technology Research Journal

Advances in Science and Technology Research Journal, 2026, 20(3), 512–524
https://doi.org/10.12913/22998624/213964
ISSN 2299-8624, License CC-BY 4.0

Received: 2025.10.15
Accepted: 2025.11.28
Published: 2026.02.01

Analysis of an energy harvesting system with kinematic excitation and step change of elastic force with hysteresis

Marek Borowiec[1*], Marcin Bocheński[1], Bartosz Drzymała[2], Mariusz Ostrowski[3]

[1] Department of Applied Mechanics, Lublin University of Technology, Nadbystrzycka 36, 20-618 Lublin, Poland
[2] Department of Electrical Drives and Machines, Lublin University of Technology, Nadbystrzycka 38a, 20-618 Lublin, Poland
[3] Institute of Fundamental Technological Research, Polish Academy of Sciences, Pawińskiego 5b, 02-106 Warsaw, Poland
* Corresponding author's e-mail: m.borowiec@pollub.pl

ABSTRACT

The efficiency of vibration-based energy harvesters is often constrained by low vibration amplitudes and limited responsiveness beyond the resonant frequency. To overcome these limitations, mechanical amplifiers and spring bumpers can be employed to enhance excitation amplitude and magnet velocity within a compact device. This study presents a nonlinear oscillator supported on pre-compressed coil springs with high-stiffness bumpers acting as motion limiters. The resulting collision effects and friction introduce hysteresis, significantly influencing the system's dynamic response. An electromagnetic model with position-dependent inductance is developed, and the identified system parameters enable numerical analysis of energy recovery and dynamic behaviour. Selected numerical predictions are compared with experimental observations, demonstrating the model's effectiveness.

Keywords: energy harvesting, nonlinear electromagnetic circuit, electromechanical systems, electromagnetic transduction, hysteresis phenomena, broadband response.

INTRODUCTION

The concept of energy harvesting from ambient sources first emerged in the second half of the 20th century, while its rapid development has been particularly evident over the past three decades. Initially, the research relied on fundamental physical effects discovered in the early 19th century, such as photoelectric, thermoelectric, and electromagnetic phenomena. A more recent principle, the piezoelectric effect – discovered in the late 19th century – has also become a cornerstone of energy harvesting technologies. These discoveries quickly inspired the development of technical devices, with Faraday's electromagnetic generator of 1831 being a notable example. The idea of miniaturizing such devices to capture mechanical energy from the environment and convert it into electrical energy suitable for powering small-scale electronic systems did not emerge until the late 20th century. One of the earliest studies in this field [1] presented a linear damped oscillator whose damping depended on the load resistance, influencing the force exerted by a coil on a magnet moving within it. This work highlighted the intrinsic limitations of systems with linear characteristics. In [2], the necessity of analysing the vibration spectrum of the environment prior to designing energy harvesters was emphasized. By 2006, one of the first comprehensive review papers had appeared [3], discussing various electromechanical solutions for powering microsystems from ambient vibrations. Systems based on piezoelectric, electrostatic, and electromagnetic transduction mechanisms were compared, and particular attention was paid to energy dissipation mechanisms. Subsequent research focused on extending the operational bandwidth of harvesters. One promising approach involved bistable systems [4, 5], where the specific form

of the potential well enabled efficient energy conversion across a wider frequency range and under stochastic excitation. It was later demonstrated [6] that double-well potential systems can generate significantly higher power levels compared to linear counterparts, due to the presence of chaotic responses. Nonlinearity was also introduced in alternative designs, such as the levitating magnet harvester described in [7], where the moving magnet was suspended between two repelling magnets instead of being supported by a spring. Both numerical modelling and experimental validation confirmed effective energy conversion across a broad frequency spectrum. In this context, the strong influence of both mechanical and electrical damping on system performance was highlighted. Among mechanical damping mechanisms, friction plays a crucial role and can substantially reduce harvesting efficiency. Some studies incorporate Coulomb's dry friction model [8, 9], while others attempt to capture more complex dependencies, such as friction varying with sliding velocity [10] or with magnet displacement inside the tube [11]. The combined dependence on displacement and velocity leads to strongly nonlinear friction models. Friction is also a major contributor to hysteretic behaviour in energy harvesting systems. Additional hysteresis effects may arise from nonlinear magnetic interactions [12, 13]. The impact of friction-induced hysteresis was analysed in [14], which showed how the shape of the hysteresis loop influences the system's dynamic response, including resonance shift and power generation efficiency. A review of the literature [12–15] indicates that hysteresis phenomena can actually be beneficial, broadening the operational bandwidth and improving energy generation under variable environmental conditions. The amount of harvested energy is closely linked to the harvester dimensions. The maximum kinetic energy of a moving magnet can be increased either by raising its mass or velocity. To enhance velocity while keeping the device compact, auxiliary springs have been proposed [16, 17], as they can store part of the magnet energy once it exceeds a certain displacement range.

The present study extends the theoretical framework developed in [17]. Based on these assumptions, a prototype harvester was constructed, and its physical parameters were experimentally identified. These parameters were then incorporated into a refined numerical model, which accounts for the nonlinear dependence of coil inductance on magnet position, replaces the previously assumed infinitely stiff springs [17] with deformable ones, and incorporates friction between the magnet and tube walls. A series of experiments was conducted for various excitation amplitudes and frequencies, including random excitations. Finally, the numerical predictions of the proposed model were compared with experimental results, demonstrating good agreement and validating the adopted approach.

Formulation of the problem

The studied model of energy harvester is shown in Figure 1. The device is made of a non-magnetic tube, locked on a rail. Inside the tube there are mounted two springs (k_1 and k_2). A moving magnet of mass m is mounted between these two springs. Each spring has two different stiffness coefficients while exerting or stretching. This phenomenon is caused by friction between the magnet and the tube and also between the spring and the tube. The laboratory stand is provided for test and to obtain the characteristics during loading and unloading cycles of the several selected springs A, B and C (see Figure 2a). The measurements revealed sudden changes of force in the system, as well as significantly different stiffness depending on the direction of the magnet's movement inside the tube (Figure 2b). Based on the actual characteristics of the spring interacting with the magnet and the tube, a linear approximation of the spring stiffness was created, represented by two straight lines with different slopes (Figure 3a). Next from the obtained stiffness characteristics, the stiffness values of applied spring were calculated k_1=335 N/m at compression and k_2=225 N/m at release. Assuming an initial compression of the springs (called d) and the use of two springs, one on each side of the moving magnet, a hysteresis characteristic was obtained, as shown in Figure 3b. As can be seen, the value of the initial compression d affects the width of the feedback loop. In the paper the results are presented and discussed for distance d=10 cm.

The system is equipped with two additional springs with stiffness k_3, which play a role as bumpers. The length of these spring bumpers is small but their stiffness k_3 is much higher than the main springs (k_1, k_2). They work when the relative output amplitude of magnet vibration crosses the distance to them, then contact occurs. Note, in the numerical model the impact is not assumed as a resilient collision. It is modelled the higher

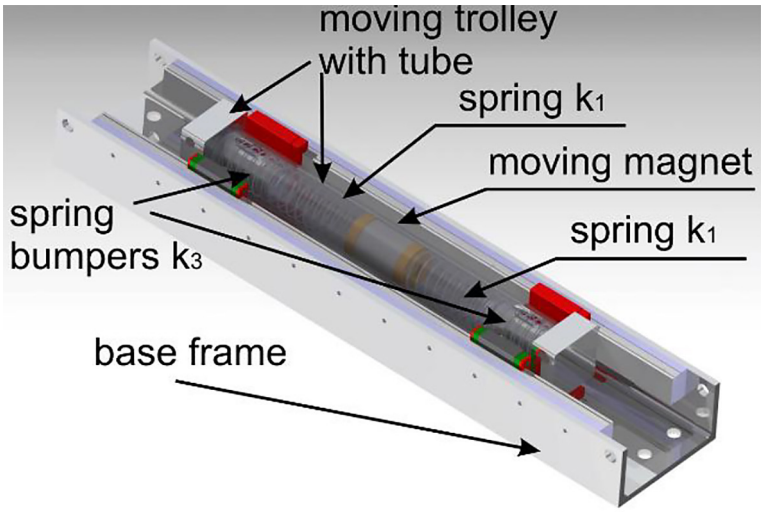

Figure 1. The oscillator with applied pre-compressed springs

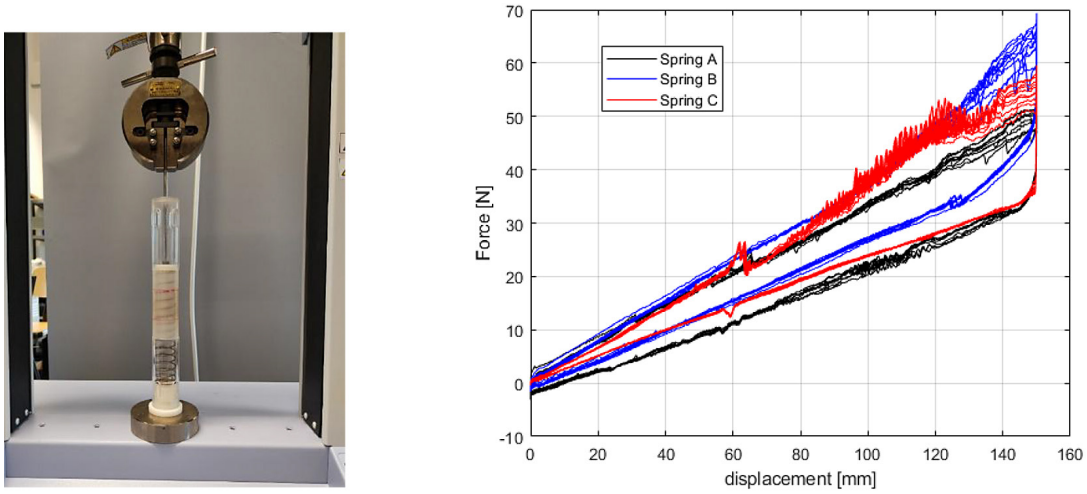

(**a**) (**b**)

Figure 2. The laboratory stand of the springs stiffness estimation (a) the measured characteristics of the selected springs (b)

stiffness springs consume the kinetic energy for potential up to moving magnet changes the velocity sign and then potential energy is releasing to kinetic one.

The subsystem of energy harvesting part consists of an electromagnetic coil attached to the tube as is schematically is shown in Figure 4. It includes a modified inductance $L(x)$ by positioning of the magnet against the coil (see Figure 5) and has the coil resistance R_c. While the mechanical system is vibrating, the electromotive force $\varepsilon_B(t)$ appears in the coil turns due to magnetic flux φ changes according the Faraday's law (Equation 1):

$$\epsilon_B(t) = -\frac{d}{dt}\Phi(x(t)) \tag{1}$$

The mechanical result of the magnetic flux gradient is the electrodynamic force done on electrical part of the system:

$$F_{el} = \frac{\partial \Phi(x)}{\partial x}\dot{q} \tag{2}$$

where: $\dot{q}$ is time derivative of the electrical charge and corresponds the electrical current in the circuit and $\frac{\partial \Phi(x)}{\partial x}$ is the electromechanical coupling, which is described by a series of trigonometric functions (Eq. (3)

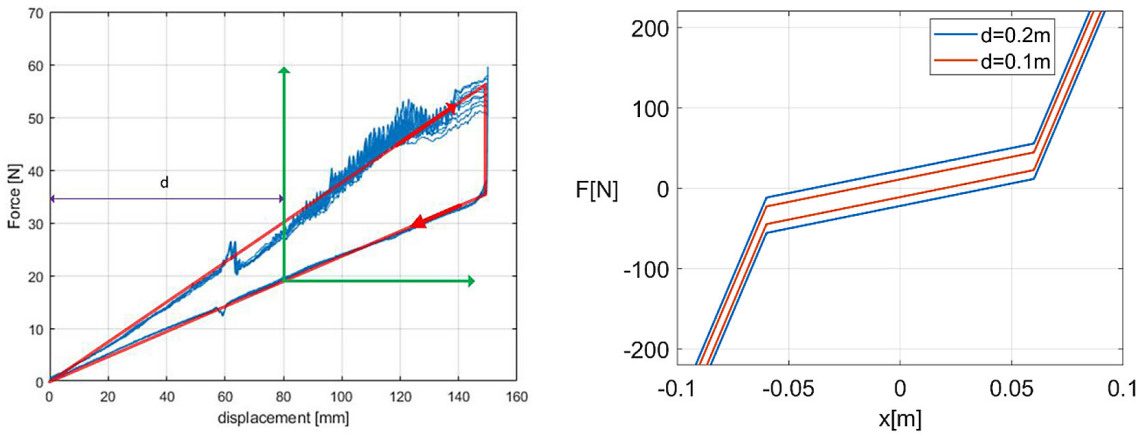

(**a**) (**b**)

Figure 3. The characteristic of the springs k_1, k_2 with applied pre-compression (a), and the force characteristic (b) at different initial compression d

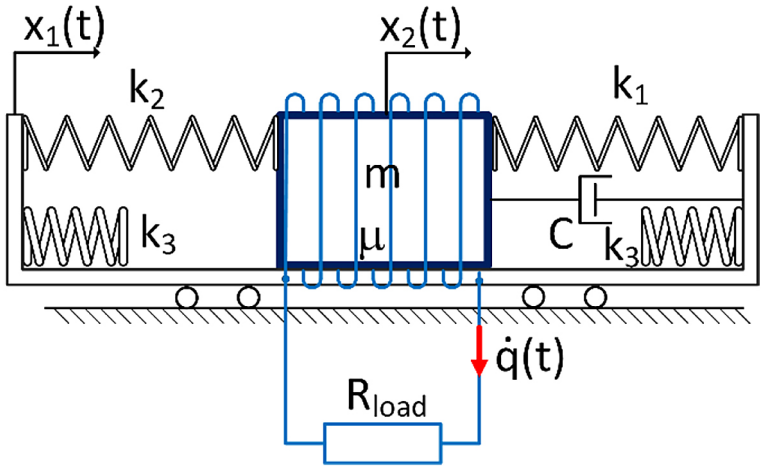

Figure 4. The schematic model of the energy harvesting oscillator

fitted to points obtained according to Biot-Savart law, as in [17].

$$\frac{\partial \Phi(x)}{\partial x} = \sum_{1}^{10} A_n \sin\left(\frac{2\pi n}{l_x} x\right) \tag{3}$$

In this study, the above equation is replaced by a fitted polynomial to facilitate simulation in the Simulink software. The value of electromechanical coupling varies due to the position of magnet within its motion length l_x=0.24 m according the curve as shown in Figure 5. For sufficient description of the curve, it has been calculated by 10 harmonics coefficients A_n. given in Table 1.

Additionally, due to possible significant magnet displacements, the reluctance force F_r on the mechanical side and the voltage varepsilon_(L_x) on the electrical side are taken into account. Both terms are described by corresponding terms:

$$F_r(x, \dot{q}) = \frac{1}{2}\frac{\partial L}{\partial x}\dot{q}^2 \tag{4}$$

$$\varepsilon_{Lx}(x, \dot{x}, \dot{q}) = \frac{\partial L}{\partial x}\dot{x}\dot{q} \tag{5}$$

Both the reluctance force F_r and voltage ε_{Lx} depend on the inductance in relation to x. The inductance of the coil at a given position x of the magnet relative to the coil $L(x)$ is expressed by Equation:

$$L(x) = L_a + \kappa_L \exp\left(-(x/\sigma_L)^2\right) \tag{6}$$

where L_a=1.63 H is coil inductance (without magnet inside), κ_L = 2.2838 H is the amplitude of the inductance variation caused

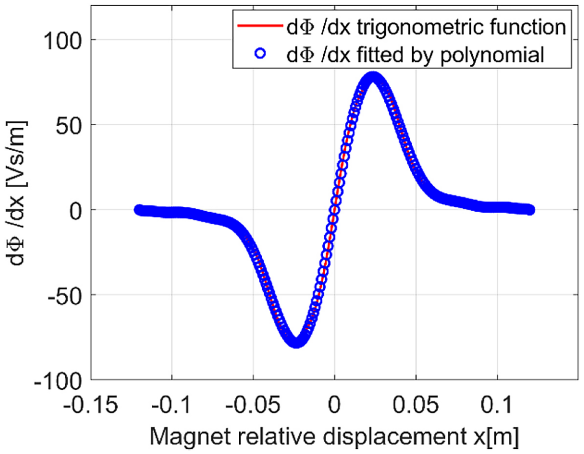

Figure 5. The electromechanical coupling as a function of magnet displacement *x*

by the presence of the magnet and σ_L = 0.0245 m describes the "width parameter" of the Gaussian curve, which determines how rapidly the inductance decreases as the magnet moves away. The magnet position for coil inductance is presented in Figure 6. Function of inductance $L(x)$ (6) is used in equations of motion (10), which is easily differentiable, decreases with displacement of the magnet and achieves zero in infinity.

The energy harvesting system was analysed in both numerical and experimental ways. To simulate the model, the differential equations of motion were provided by Lagrange approach:

$$\mathbb{L} = T + M - \Pi - E = \frac{1}{2}m(\dot{x}_2 + \dot{x}_1)^2 + \frac{1}{2}L(x)\dot{q}^2 + \phi(x)\dot{q} - \frac{1}{2}kx^2 \tag{7}$$

In the Equation 7, *T* and *M* mean kinetic and magnetic energies, respectively but *Π* and *E* correspond to mechanical and electrical potential energies. Here, the electrical potential energy is zero. The energy exchange between electrical and mechanical parts of the system due to magnetic field of the vibrating magnet is expressed by term $\phi(x)\dot{q}$ in magnetic energy and relates to the mechanical work of the force F_{el}.

According the schematic presented in Figure 4, the mechanical part is a one degree of freedom where the generalized coordinate is the displacement *x* between the magnet (x_2) and the tube (x_1). The second degree of freedom comes from the electrical part and it is an electric charge $q(t)$. Finally in the Euler–Lagrange equations with included the conservative and dissipative forces are the form:

$$\begin{cases} \frac{d}{dt}\frac{\partial \mathbb{L}}{\partial \dot{x}} + \frac{\partial \mathbb{D}}{\partial \dot{x}} - \frac{\partial \mathbb{L}}{\partial x} = 0 \\ \frac{d}{dt}\frac{\partial \mathbb{L}}{\partial \dot{q}} + \frac{\partial \mathbb{D}}{\partial \dot{q}} - \frac{\partial \mathbb{L}}{\partial q} = 0 \end{cases} \tag{8}$$

where: dissipation function $\mathbb{D}$ contains the power of the energy losses in the system:

$$\mathbb{D} = \frac{1}{2}c\dot{x}^2 + \frac{1}{2}R_c\dot{q}^2 \tag{9}$$

After substitution the equations of Lagrangian (7) and dissipation function (9) into the Euler – Lagrange Equations 8, the differential equation of motion reached form as below:

$$\begin{cases} m\,\ddot{x}_2 + c\dot{x} + R_1 + R_2 + F_t - \\ -\frac{1}{2}\frac{\partial L(x)}{\partial x}\dot{q}^2 - \frac{\partial \Phi(x)}{\partial x}\dot{q} = 0 \\ L(x)\ddot{q} + (R_c + R_{load})\dot{q} + \\ + \frac{\partial L(x)}{\partial x}\dot{q}\dot{x} + \frac{\partial \Phi(x)}{\partial x}\dot{x} = 0 \end{cases} \tag{10}$$

Because of the excitation $x_1 = x_e \sin(2\pi f t)$ acts on the magnet is kinematic only, the right hand side of the Equation 10 equal zero. The differential Equation 10 contain nonlinearities associated with the dependence of the inductance and electromechanical coupling on relative displacement of the moving magnet x_2, and there are electromotive force due to moving magnet (Equation 1), electrodynamic force (Equation 2), reluctance force (Equation 4) and also the derivative of magnetic flux linkage induced by the current in the coil over the time (Equation 5). Moreover, in the mechanical part of differential equation of motion one can distinguish three forces. The first force R_1 (Equation 11) corresponds to the two compressed

Table 1. The coefficients of series for electromechanical coupling

A_n [Vm/s]	A_1	A_2	A_3	A_4	A_5	A_6	A_7	A_8	A_9	A_{10}
Values	31.6332	34.6694	22.4439	8.6255	1.1623	-0.7911	0.2318	1.0248	1.0689	0.3494

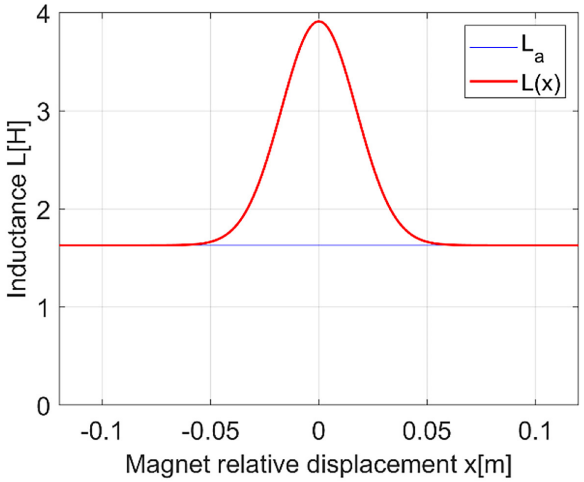

Figure 6. The curve of coil inductance $L(x)$ against the magnet position

Table 2. The parameters of the system

Descriptions	Values
Magnet material	NdFeB (N38)
Magnet height	h_m = 35 mm
Magnet diameter	d_m = 30 mm
Magnet mass	m = 0.205 kg
Coil wire resistance	R_c = 6500 Ω
Electric load	R_{load} = 5600 Ω
Coil inductance (without magnet inside)	L_a = 1.63 H
Number of coil turns	N = 8000
Wire diameter	d_w = 0.06 mm
Axial length of the coil	h_c = 45 mm
Outer diameter of the coil	D_c = 42 mm
Inner diameter of the coil	d_c = 40 mm

springs of stiffness k_1 and k_2 working all the vibrating time, the second force R_2 appears at moving magnet crossed through the threshold distance TR = 0.06 m and activates the spring with high stiffness k_3 according to the Equation 12. The third called friction force F_t depends on the distance d which keeps the hysteresis effect of both pre-compressed springs k_1 and k_2 (Equation 13):

$$R_1 = (k_1 + k_2)x \tag{11}$$

$$R_2 = \begin{cases} k_3(x + TR)\ if\ x < -TR \\ k_3(x - TR)\ if\ x > +TR \\ 0\ if\ -TR \le x \le +TR \end{cases} \tag{12}$$

$$F_t = (k_1 - k_2)d \begin{cases} +F_t, \dot{x} \ge 0 \\ -F_t, \dot{x} < 0 \end{cases} \tag{13}$$

The sum forces expressed by Equation 10, 11, 13 is plotted in Figure 3b. and denoted by Equation 14 as below:

$$F = R_1 + R_2 + F_t \tag{14}$$

RESULTS OF THE NUMERICAL MODEL

The results for discussed analytical model are provided for parameters listed in Table 2. The values of them are taken from the real system presented in the next section of experimental analysis. Based on the differential equation of motion, the numerical system are created in Simulink software (Figure 7). The simulations procedure are provided by integration method of Runge-Kutta 4th order at fixed time steps. For each input parameters, the final results are taken for steady-state response.

The efficiency of the system strongly depends on the damping coefficient and bumpers characteristic. The influence of both inputs parameter were analysed, bumpers stiffness k_3 and damping c on the output amplitude and voltage are presented in Figures 8(a, b). The range of k_3 and c are taken from 0 to 10000 N/m and from 0 to 20 Ns/m, respectively. It showed the possible relative efficiency of the system for energy harvesting. Based on the analysis for system sensitivity onto these parameters, both values for numerical simulations are fixed k_3=6000 N/m and c=8 Ns/m. For assumed parameters the output amplitude and voltage are simulated in the vicinity of the first resonance zone up to 15 Hz as shown in Figures 9.

The first resonance is significant for energy harvesting device system and the simulated results provided the voltage increasing at relatively high the excitation acceleration. The behaviour of the harvester is presented for selected excitation forces ranging from 15 g up to 40 g. Each of four excitation level confirms the energy harvesting efficiency is focused within the first resonance zone, it exhibits a distinct resonance in the 10–14 Hz range. Higher excitation values lead to greater response amplitudes, which may suggest nonlinear system behaviour. Apart from the main resonance, the system shows additional smaller peaks, suggesting the existence of multiple natural frequencies or complex dynamic effects.

In Figure 9a one can easily notice the range of both, force and frequency excitation levels,

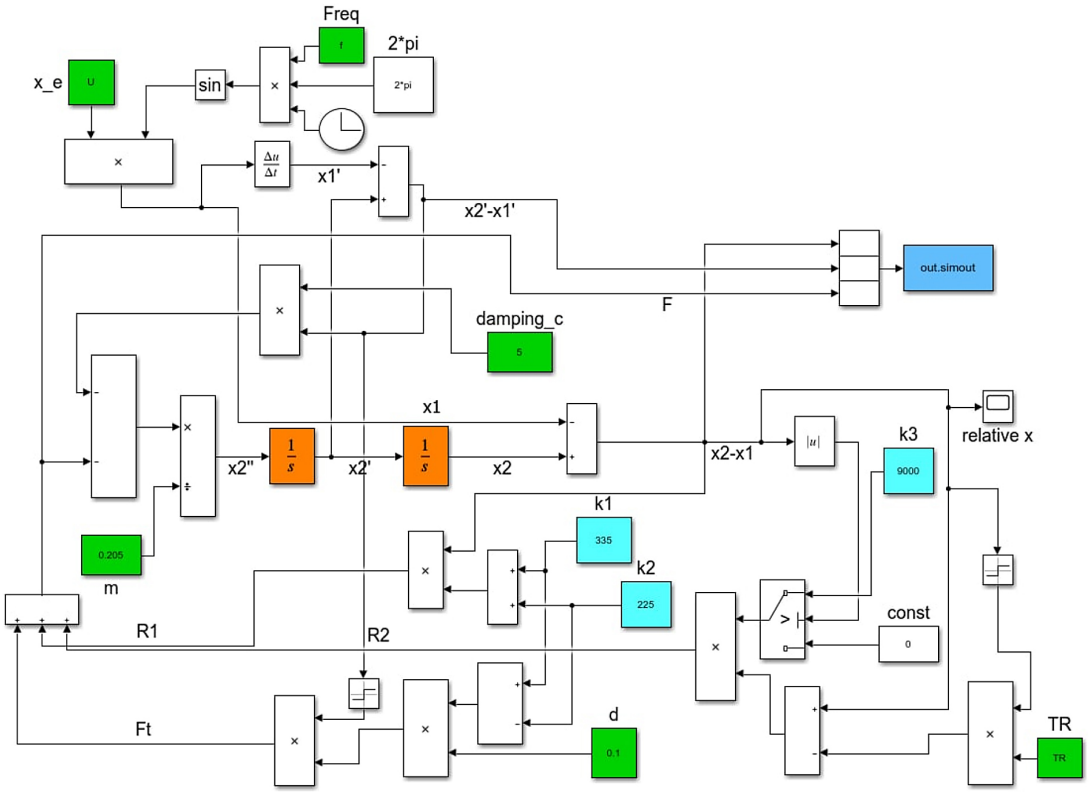

Figure 7. The numerical model based on Simulink structure

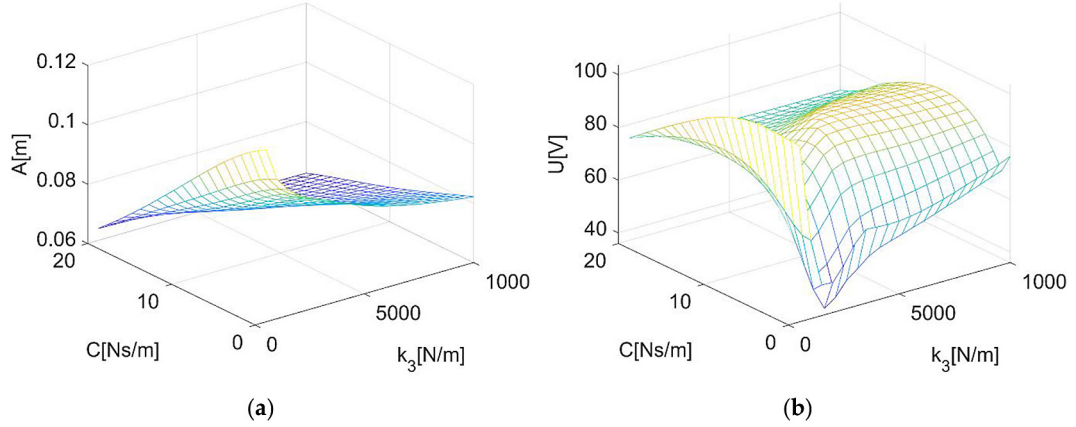

Figure 8. Influence of the additional spring's stiffness k_3 and the damping C on the system response. Figure a and b are plotted for a_{exc}=40 g and excitation frequency f=5 Hz, where $a_{exc}=x_e(2\prod f)^2$

beyond which the system enters to the bumpers activation. This range is limited in the region where the magnet movement exceeds the threshold distance *TR*. It is the excitation frequency f = 0 Hz – 14 Hz and the excitation acceleration a_{exc} =18 g – 40 g detailed by rectangular area in Figures 9a. The bumpers activation causes a change in the voltage characteristics (see Figure 9c, d) and at a_{exc} = 18 g it is visible a gentle jump by f = 4.5 Hz which finally leads to double peaks at 5 Hz and the within 11.5–13.5 Hz, depending on the excitation level. Then, the system with active bumpers operates over a wider resonance zone, increasing its energy-harvesting efficiency.

Moreover, the increasing of excitation amplitude from 15 g to 40 g causes the increasing of output voltage appeared at higher excitation frequencies (see Figure 9d). It means the higher input amplitude, the more efficient system becomes despite the fact that the output amplitude keeps relatively constant value in whole range of resonance zone between 2 Hz – 14 Hz.

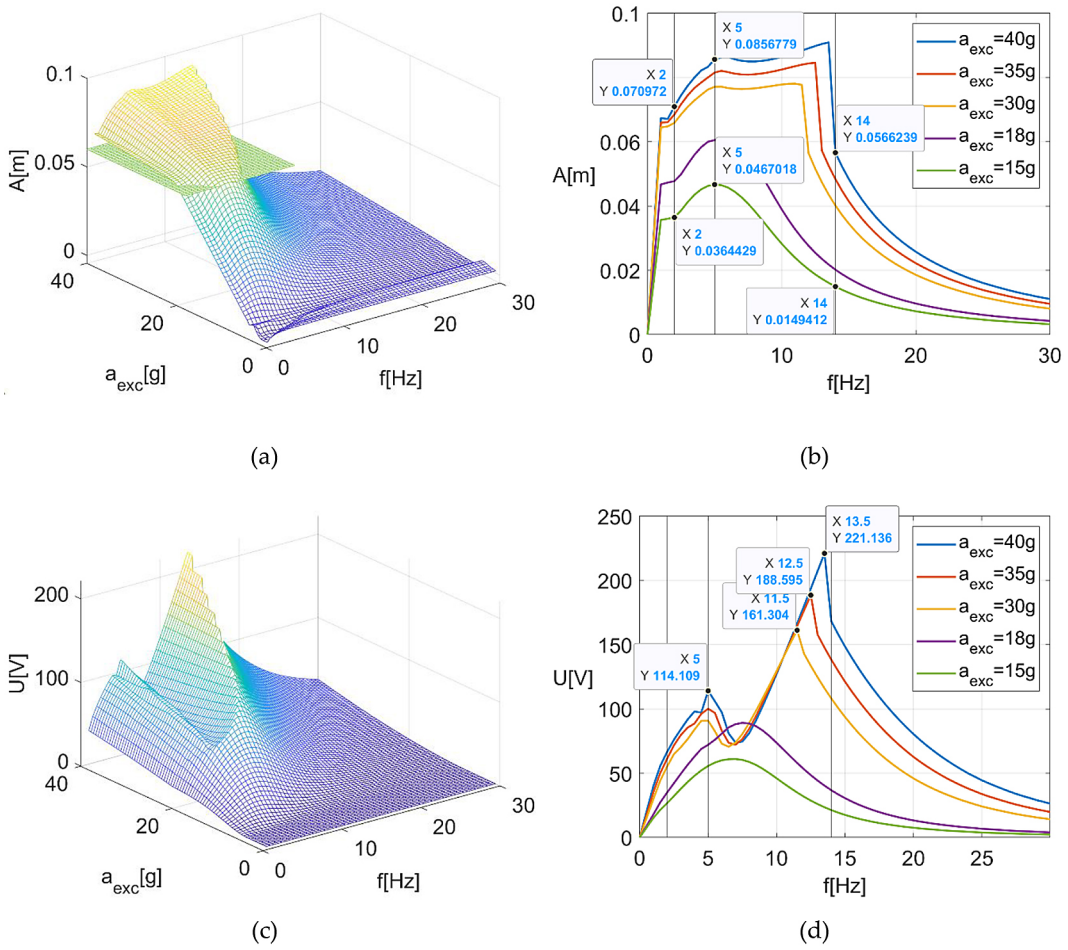

Figure 9. The influence of the excitation amplitude *g* and frequency *f* on the amplitudes of magnet displacement (a) and voltage response (c), and their 2D visualisation for selected amplitudes of excitation (b) and (d), respectively

The visualisation of the system behaviour is provided by the time series for chosen three points of excitation frequencies 2 Hz, 5 Hz and 14 Hz (Figures 9b, 9d). In Figures 10a-f is shown the characteristics at two extreme excitation levels a_{exc} = 15 g and a_{exc} = 40 g, where the first level corresponds to operation without impacts, while the second involves bumper activation with impact effects. The series are compared at excitation frequencies before the resonance zone f = 2 Hz, inside it = 5 Hz, and the above the zone f = 14 Hz. In each cases the response amplitudes of the system are higher at excitation acceleration a_{exc} = 40 g, what is obvious but the relation differs. For the last case at excitation 40 g (Figure 10e) the output amplitude is three times higher than at 15 g, simultaneously without impacts. It is significantly different behaviour from the two previous at 5 Hz and 2 Hz (Figure 10a, c) where the relation of output amplitudes are less than two times in spite of the impacts appeared. One can conclude, the higher excitation amplitude at frequency above the resonance zone, reveals the response system at enough small amplitude to avoid the impacts what is visible both, in the amplitude and voltage time response. From a technical point of view, the higher resonance frequencies ensure three times higher output voltages in the electrical subsystem.

Experimental investigation

In this section, the numerical results simulated by numeric model are verified. Dynamic tests were performed on an experimental model designed according to the layout shown in Figure 1. To verify the effectiveness of the energy harvester, two excitation sources were proposed to reproduce a wide range of forcing amplitudes. The first source was the electromagnetic shaker TIRA 50101 (Figure 11a) with an LMS Scadias III controller and Test.Lab 14A software, providing specific environmental conditions for

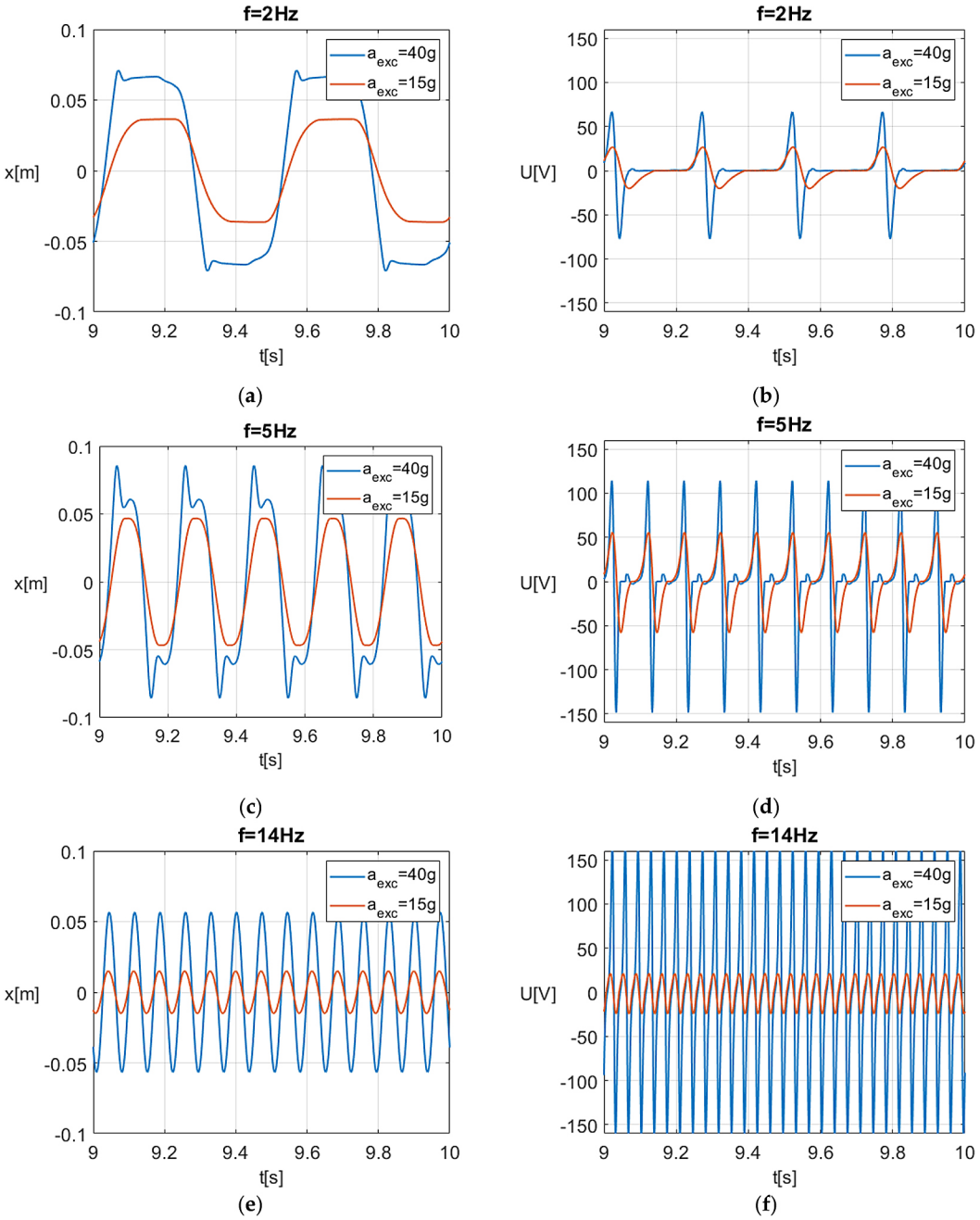

Figure 10. The amplitude displacements (a, c, e) and voltage (b, d, f) responses of the system at chosen excitation frequencies f = 2 Hz, f = 5 Hz and f =14 Hz. The excitation acceleration chosen for comparison are 15 g and 40 g

the oscillator. However, due to limitations of maximum force and displacement in this excitation source, the excitation amplitudes are not able to exceed 15 g within the frequency range, moreover it significantly decreased at low frequencies. The second system consists of the asynchronous motor with a variable eccentricity, controlled by an electronic inverter (Figure 11b). This system allowed overcoming the limitations of the electromagnetic shaker, enabling higher forcing amplitudes at both low and high frequencies. Unfortunately, the excitation deviated slightly from a sinusoidal form due to the use of the eccentric.

Additionally, the shaker combined with the control system permitted the study of the system's response to random excitations. The system response here refers to the time histories of the voltage generated across the applied resistive load. The noise excitation was used to compare

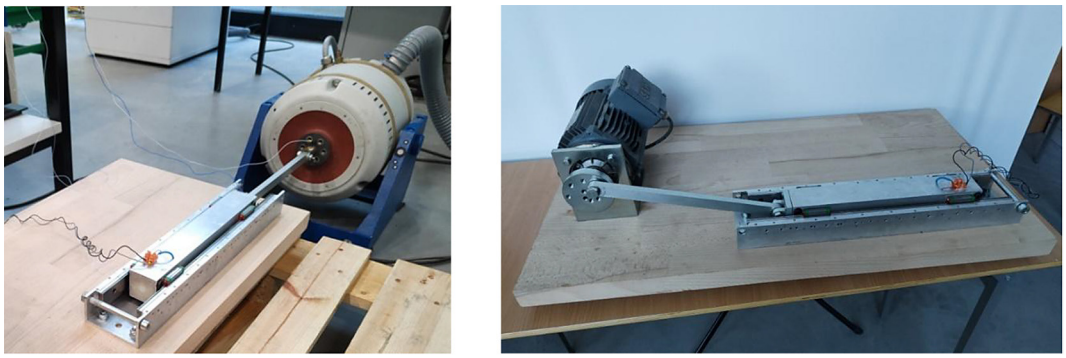

(**a**) (**b**)

Figure 11. The laboratory stands of the energy harvesting device jointed to the excitation sources provided by electrodynamical shaker (a) and electric motor (b)

the laboratory response of model with the theoretical results presented in the work [17].

In the first stand with applied shaker an excitation with an RMS intensity of 2 g was applied over a frequency range from 5 to 120 Hz (Figure 12a) and the system response is presented in Figure 12b. The highest voltages are generated by the harvester within the frequency range of 5–35 Hz. Subsequently, as the frequency increases, the values of the generated voltages decrease. The wide range of useful excitation frequencies for the laboratory model confirms the conclusions obtained theoretically in the work [17].

The results of the tests with motor excitation showed that the second harmonic plays a significant role in the system response, despite the excitation system generating mainly odd harmonics (Figures 13). At the excitation frequency 7 Hz, where contact between the magnet and the additional springs had not yet occurred, the contribution of successive harmonics in the coil voltage signal gradually decreases. It reveals the highest system efficiency of energy harvesting occurs mainly in the vicinity of the first resonance, but at higher excitation frequency it gradually disappears. At excitations of 15 Hz and 20 Hz, when

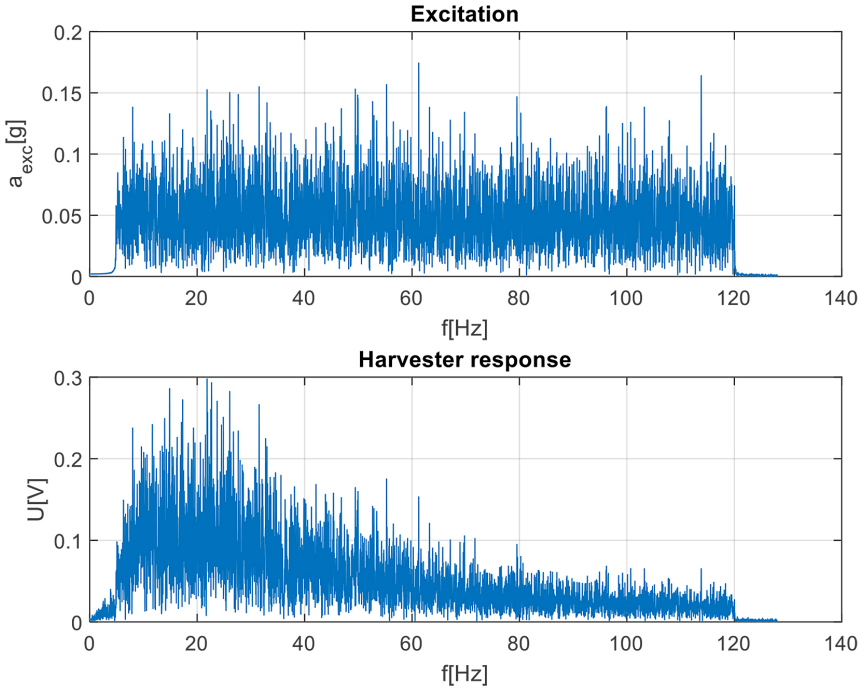

Figure 12. The experimental results at random excitations spectrum generated by shaker (a), and harvester response (b)

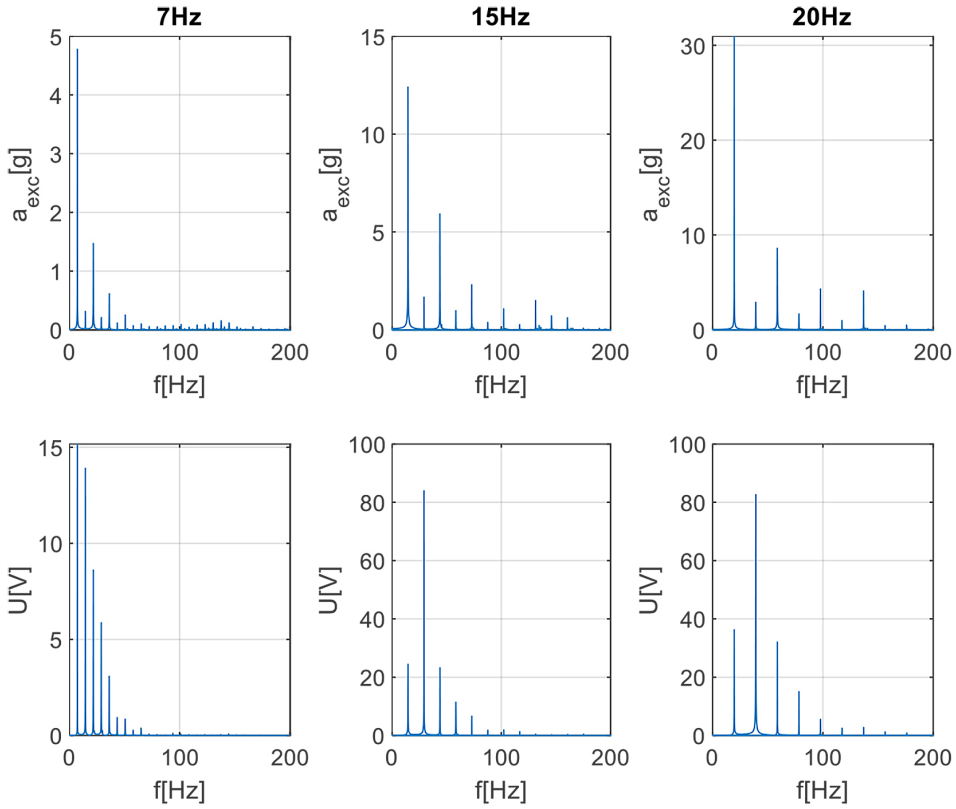

Figure 13. The spectra responses of laboratory tests at AC motor excitation approach, the acceleration of harvester tube (a) and the voltage generated on the load resistor (b)

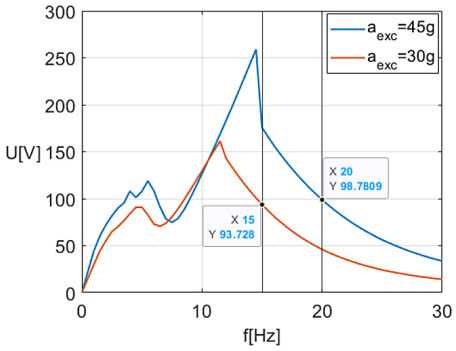

(a)

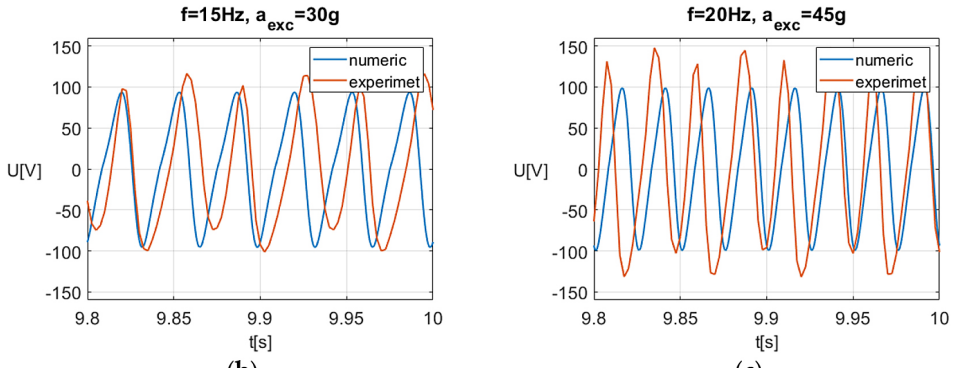

(b) **(c)**

Figure 14. The amplitude – frequency results of the escalator system (a) and the time series of voltage response comparison at excitation inputs for f = 15 Hz, a_{exc} = 30 g (b) and for f = 20 Hz, a_{aexc} = 45 g (c)

the magnet hits the additional springs, the second harmonic clearly dominates over the others, including the fundamental frequency. It confirms, the activation of the extra springs broaden the zone, where the energy harvesting efficiency is kept. Finally, as visible in Figure 13 the output voltage U is increased in wide range of excitation frequency exceeding 20 V and even in some frequency is gone up to 80 V.

In the last Figure 14, the comparison of experimental and numerical results are plotted. There are presented both, amplitude – frequency results (Figure 14a) and the time series responses (Figure 14b, 14c) for fixed excitation frequencies 15 Hz, 20 Hz and amplitudes levels at 30 g and 45 g, respectively. These correspond to the achieved experimental result reached at slight above the resonance zone due to the kinematics of the real system mechanism. The verification of the numerical response of voltage time series is relatively in accordance to experimental output voltage both in qualitative and quantitative point of view. One can see the sinusoidal behaviour of the voltage series which reproduce the characteristics of excitation force from the eccentricity mechanism.

CONCLUSIONS

Summarising, the energy harvester exhibits the highest efficiency within the first resonance zone, particularly for excitation frequencies in the range of 10–14 Hz. In this range, both the displacement amplitude and the output voltage reach their maximum values. As far as the influence of the spring bumpers in concerned, the activation of additional high-stiffness spring bumpers extends the resonance zone and increases the generated voltage. This occurs when motion of the magnet exceeds the threshold distance (TR = 0.06 m), causing impacts that enhance the energy harvesting capability of the oscillator.

Additionally, one can conclude, the system shows strongly nonlinear behaviour. Multiple peaks in the voltage and amplitude response suggest the presence of additional natural frequencies and complex dynamics. Hysteresis effects due to friction and asymmetric spring characteristics further contribute to the nonlinear response.

Under motor-driven excitation, the second harmonic dominates the response of the system at frequencies of 15 Hz and 20 Hz, despite the excitation mechanism primarily generating odd harmonics. This indicates that the impacts between the magnet and bumpers play a crucial role in shaping the voltage signal. Experimental results obtained under both random and harmonic excitations are in good agreement with numerical simulations, confirming the validity and predictive capability of the proposed mathematical model. Analysed the dependence on excitation amplitude, increasing it from 15 g to 40 g leads to higher output voltages, even if the displacement amplitude remains nearly constant. This demonstrates that the system becomes more efficient at higher excitation levels, especially at frequencies near or above resonance.

Acknowledgments

This research was funded by the National Science Centre, under the OPUS-26 call in the Weave programme, ATEKNEHT UMO-2023/51/I/ST8/02739.

REFERENCES

1. Williams, C.B.; Yates, R.B; Analysis of a micro-electric generator for microsystems. Sensors and Actuators A: Physical, 1996; 52: 8–11, https://doi.org/10.1016/0924-4247(96)80118-X
2. Shad, R.; Wright, P. K.; Rabaey, J.; A study of low level vibrations as a power source for wireless sensor nodes, Computer Communications, 2003; 26(11): 1131–1144, https://doi.org/10.1016/S0140-3664(02)00248-7
3. Beeby, S. P.; Tudor, M. J.; White, N. M.; Energy harvesting vibration sources for microsystems applications, 2006; 17(12), Measurement Science & Technology, https://doi.org/10.1088/0957-0233/17/12/R01
4. Cottone, F.; Vocca, H; Gammaitoni, L. Nonlinear energy harvesting. Phys Rev Lett. 2009 Feb 27; 102(8): 080601(1–4). https://doi.org/10.1103/PhysRevLett.102.080601
5. Gammaitoni, L.; Neri, I.;, Vocca, H. Nonlinear oscillators for vibration energy harvesting, Applied Physics Letters, 2009. https://doi.org/10.1063/1.3120279
6. Erturk, A.; Hoffmann, J.; Inman, D. J.; A piezomagnetoelastic structure for broadband vibration energy harvesting, Applied Physics Letters. 2009; 94(25). https://doi.org/10.1063/1.3159815
7. Mann, B.P; Sims, N.D. Energy harvesting from the nonlinear oscillations of magnetic levitation, Journal of Sound and Vibration, 2009; 319(1–2):

515–530, https://doi.org/10.1016/j.jsv.2008.06.011

8. Berdy, D.F; Valentino, D.J; Peroulis, D. Design and optimization of a magnetically sprung block magnet vibration energy harvester, Sensors and Actuators A: Physical, 2014; 218: 69–79, https://doi.org/10.1016/j.sna.2014.06.011
9. Kanj, A.; Thanalakshme, R.P.;, Li, Ch.; Kulikowski, J.; Bahl, G.; Tawfick, S. Design, dynamics, and dissipation of a torsional-magnetic spring mechanism, Mechanical Systems and Signal Processing, 2022; 179, https://doi.org/10.1016/j.ymssp.2022.109307
10. Zhao, H.; Ouyang, H. Structural and electrical dynamics of a grating-patterned triboelectric energy harvester with stick–slip oscillation and magnetic bistability. Nonlinear Dyn, 2022; 109: 479–506. https://doi.org/10.1007/s11071-022-07230-y
11. Kecik, K..; Mitura, A. Effect of variable friction on electromagnetic harvester dynamics. Eur. Phys. J. Spec. Top. 2022; 231: 1433–1441. https://doi.org/10.1140/epjs/s11734-022-00493-x
12. Lin, J-T.; Lee, B.; Alphenaar, B.W. The magnetic coupling of a piezoelectric cantilever for enhanced energy harvesting efficiency. Smart Materials and Structures. 2010; 19: 045012. https://doi.org/10.1088/0964-1726/19/4/045012
13. Stanton, S.C.; McGehee, C.C.; Mann, B.P. Reversible hysteresis for broadband magnetopiezoelastic energy harvesting. Applied Physics Letters. 2009; 95: 174103. https://doi.org/10.1063/1.3253710
14. Semenov, M.E.; Meleshenko, P.A.; Borzunov, S.V.; Reshetova, O.O.; Barsukov, A.I. A simple model of the energy harvester within a linear and hysteresis approach. Micromachines. 2023; 14(2): 310. https://doi.org/10.3390/mi14020310
15. Chen, W.; Mo, J.; Ouyang, H.; Xiang Z.; Zhao J. A bistable energy harvester for friction-induced stick–slip vibration. Nonlinear Dyn. 2024; 112: 353–378. https://doi.org/10.1007/s11071-023-09055-9
16. Haroun, A.; Yamada, I.; Warisawa, S. I. Micro electromagnetic vibration energy harvester based on free/impact motion for low frequency–large amplitude operation. Sensors & Actuators A: Physical. 2015; 224: 87–98. https://doi.org/10.1016/j.sna.2015.01.025.
17. Ostrowski, M.; Błachowski, B.; Bocheński, M.; Piernikarski, D.; Filipek, P.; Janicki, W. Design of nonlinear electromagnetic energy harvester equipped with mechanical amplifier and spring bumpers. Bulletin of the Polish Academy of Sciences: Technical Sciences, 2020; 68(6): 1373–1383, https://doi.org/10.24425/bpasts.2020.135384